Revised Chlorophyll-a Algorithms for Satellite Ocean Color Sensors in the East/Japan Sea

Jongseong Ryu[1], SeungHyun Son[2,3,*], Chun Ok Jo[4], Haecheol Kim[5], Yonghoon Kim[6], Sang Heon Lee[7], and HuiTae Joo[8]

[1] Department of Marine Biotechnology, Anyang University, Incheon, Republic of Korea

[2] NOAA/NESDIS Satellite Applications and Research, College Park, MD, USA

[3] CIRA, Colorado State University, Fort Collins, CO, USA

[4] OceanScitech, Inc., Seoul, Republic of Korea

[5] SAIC at NOAA/NESDIS/EMC, Princeton, NJ, USA

[6] Department of Earth and Space Sciences, West Chester University of Pennsylvania, West Chester, PA, USA

[7] Department of Oceanography and Marine Research Institute, Pusan National University, Pusan, Republic of Korea

[8] National Institute of Fisheries Science, Busan, Republic of Korea

*. E-mail: ssonocean@gmail.com

ABSTRACT

The East/Japan Sea (hereafter, East Sea (ES)) is a semi-enclosed marginal sea and considered as a miniature ocean with oceanic features (e.g., currents, eddies, fronts, upwelling) and dynamic marine environments. The ES is significantly influenced by the global ocean warming with fast increases in sea surface temperature during the last several decades. The climate-induced environmental changes can affect marine ecosystem and food webs in the ES. Therefore, more accurate estimates in phytoplankton biomass in the ES with high spatial and temporal resolutions are necessary to investigate phytoplankton production, fisheries, and carbon budget as well as biological responses to the environmental and climate changes. The NASA ocean chlorophyll-type (OCx) chlorophyll-*a* (Chl-*a*) algorithms based on blue to green band ratio for the satellite ocean color data in the global ocean have been evaluated using the in situ radiometric and Chl-*a* measurements in the ES. The model-derived Chl-*a* data using the OC Chl-*a* algorithms present systematic overestimation in the lower Chl-*a* concentrations between about 0.1 and 1.0 mg/m^3 in the ES (with ~40% uncertainties). New Chl-*a* algorithms for the ES has been derived from the 3^{rd} polynomial regression fits of in situ Chl-*a* and maximum band ratios of remote sensing reflectance (R_{rs}). The revised Chl-*a* algorithms considerably improve the Chl-*a* data in the ES from the satellite ocean color data in the lower Chl-*a* concentrations. Thus, the new Chl-*a* algorithms can provide more accurate assessments in biological and biogeochemical processes such as primary productivity, phytoplankton phenology, phytoplankton dynamics, and carbon cycles.

Key words: Ocean Color Remote Sensing, Chlorophyll-a, East/Japan Sea

1. INTRODUCTION

Phytoplankton form the base of the aquatic food web. The phytoplankton blooms can affect the species composition, abundance, and diversity of marine organisms in the upper levels of the food web (Ardyna and Arrigo 2020). Through photosynthesis, phytoplankton also play essential roles in transferring CO_2 to the surface ocean from the atmosphere. The organic carbon produced by photosynthesis is exported into the deep waters, influencing the carbon cycles in the ocean. Because of their far-reaching importance on the ecosystem and carbon cycles, many researchers have been studying the dynamics and phenology of phytoplankton and estimating primary productivity (Ardyna and Arrigo 2020; Chen et al. 2017; Sapiano et al. 2012). Satellite ocean color sensors provide chlorophyll-*a* (Chl-*a*) concentrations, the principal photosynthetic pigment commonly found in all phytoplankton, with high temporal and spatial resolutions. The Chl-*a* concentrations, as an indicator of phytoplankton biomass, have been used to investigate phytoplankton dynamics and estimate primary productivity in various aquatic ecosystems (Chen et al. 2017; Sapiano et al. 2012).

The East/Japan Sea (hereafter, East Sea (ES)) is typical of a semi-enclosed marginal sea. But it has been often referred to as a miniature ocean due to its oceanic features such as basin-scale gyres, deep-water formation, and thermohaline circulation (Chang et al. 2009; Kim et al. 2001). In this respect, the ES is regarded as an optimal region for monitoring physical and biological responses to climate changes (e.g., Kim et al. 2008; Lee et al. 2009). Recently, the ES showed 2-3 times faster increases in sea surface temperature than the global ocean during the last 51 years (Han and Lee 2020). Indeed, the primary productivity of phytoplankton can be strongly related to

66 abundance of commercially important fish species in the ES (Lee et al. 2018; 2019). Moreover,
67 the Chl-a concentration can be important in the local distribution of common Mink Whale in the
68 ES (Lee et al. 2017). Recently, Lee et al. (2022) reported that potential fishery can be variable
69 depending on the primary production of phytoplankton through physical and chemical structures
70 in the ES ecosystem since lower Chl-a concentration could be expected with increasing water
71 temperature (Joo et al. 2017). It is expected to significantly affect phytoplankton in the base of the
72 food web of the ecosystem. Therefore, it is necessary to gain insights into spatial and temporal
73 distributions of phytoplankton biomass and primary productivity and phytoplankton phenology in
74 the ES to understand responses to environmental and climate changes. Many prior studies have
75 been using the Chl-*a* concentrations derived from ocean color to investigate spatial and temporal
76 variations of phytoplankton biomass in the ES and relationships between their variations and
77 environmental factors (e.g., Ashjian et al. 2006; Jo et al. 2014; Kim et al. 2000; Lee et al. 2014;
78 Yamada et al. 2004). The timings of the onset of the spring bloom have been derived from the
79 satellite-derived Chl-*a* data to understand phytoplankton dynamics and phenology (Jo et al. 2007;
80 Maúre et al. 2017; Yamada et al., 2004). The Chl-*a* concentrations have also been used as key
81 variables to calculate primary productivity (Joo et al. 2014, 2016; Son et al. 2005; Yamada,
82 Ishizaka, and Nagata 2005) and export production ratios in the ES (Jo et al. 2021).

83 Ocean color remote sensing data (e.g., Moderate Resolution Imaging Spectroradiometer
84 (MODIS) on Aqua, Visible Infrared Imaging Radiometer Suite (VIIRS) on the Suomi National
85 Polar-orbiting Partnership (SNPP), Ocean and Land Color Instrument (OLCI) on the SENTINEL-
86 3, Geostationary Ocean Color Imager I and II (GOCI-1, GOCI-2)) can estimate Chl-*a*
87 concentrations reasonably well in the global open ocean waters using the NASA Ocean Color (OC)

chlorophyll-type (OCx) approach based on empirical relationship from Chl-*a* measurements and blue-green reflectance ratios (O'Reilly et al. 1998, 2000) as the NASA OC Chl-*a* algorithms. However, it has been reported that there are systematic uncertainties in the satellite estimation of Chl-*a* by oceans (e.g., Atlantic, Pacific, Indian, and Southern Oceans) because of their optical differences possibly due to phytoplankton community structure or biogeochemical processes (Szeto et al. 2011). Thus, in this study, we evaluate the performance of the existing Chl-*a* algorithms for the various satellite ocean color data in the ES with the in situ measured radiometric and chlorophyll-a data. Then we derive revised Chl-*a* algorithms for the satellite ocean color data in the study area. Finally, we implement the revised Chl-*a* algorithms to the satellite ocean color data to provide improved Chl-*a* products in the ES.

2. DATA and METHODS

2.1. SeaBASS in situ measurements

All available in situ radiometric data, remote sensing reflectance ($R_{rs}(\lambda)$), and Chl-*a* data in the ES (Fig. 1) were downloaded from the SeaWiFS Bio-optical Archive and Storage System (SeaBASS) database website (https://seabass.gsfc.nasa.gov/) maintained by the NASA Goddard Flight Space Center's Ocean Biology Processing Group (OBPG) (Werdell et al. 2002, 2003) to evaluate the current ocean color Chl-*a* algorithms for the satellite ocean color remote sensing data and improve the Chl-*a* algorithms in the ES. Total number of the available data set including the in situ ($R_{rs}(\lambda)$) and Chl-*a* measurements is 53 since 1999 (24 in June–July 1999, 11 in April 2001, and 18 in May 2016). Those measurements are processed following to the special requirements from the SeaBASS including data calibration. More detailed information of the measurements and processing methods can be found in the SeaBASS website (https://seabass.gsfc.nasa.gov/). The $R_{rs}(\lambda)$ data were interpolated with 1 nm interval and $R_{rs}(\lambda)$ at the following wavelengths are used in this study for the satellite ocean color sensors, MODIS-Aqua (443, 488 and 547 nm), VIIRS-

SNPP (443, 486 and 551 nm), GOCI-1, GOCI-2 (443, 490, 510, and 555 nm), and OLCI (443, 490, 510 and 560 nm).

To evaluate the performance of the Chl-*a* algorithms based on the maximum band ratio (MBR) of blue to green band for the satellite ocean color data (KIOST 2021*;* Morel and Antoine 2011; Morel et al. 2007a, 2007b; O'Reilly et al. 1998, 2000), five Chl-*a* OCx algorithms for MODIS-Aqua, VIIRS-SNPP, OLCI, GOCI-1, and GOCI-2 were applied to the SeaBASS in situ $R_{rs}(\lambda)$ measurements in the ES. The in situ Chl-*a* measurements were compared with the model-derived Chl-*a* using OC3M for MODIS-Aqua (O'Reilly et al. 1998, 2000), OC3V for VIIRS-SNPP (O'Reilly et al. 1998, 2000), OC4Me for OLCI (Morel and Antoine 2011; Morel et al. 2007a, 2007b), OC3G and OC4G for both GOCI-1 and GOCI-2 (KIOST 2021) in the ES (Table 1 and Fig. 2).

2.2. Satellite Ocean Color data

To compare the satellite-derived Chl-*a* images using the OC Chl-*a* algorithms with those using revised Chl-*a* algorithms for the ES, MODIS-Aqua and VIIRS-SNPP ocean color data were used. The MODIS-Aqua and VIIRS-SNPP Level-2 daily ocean color products including Chl-*a* concentration and $R_{rs}(\lambda)$ were downloaded from the NASA OBPG (http://oceancolor.gsfc.nasa.gov/) in June 2016. Both MODIS-Aqua and VIIRS-SNPP level-2 ocean color data were processed using the atmospheric correction algorithm using the near infrared (NIR) radiance corrections (Bailey, Franz, and Werdell 2010; Stumpf et al. 2003). First, three Level-2 data flags (high sun glint, high sensor-zenith angle and high solar-zenith angle) were applied to both MODIS Aqua and VIIRS SNPP Level-2 data. The present and revised Chl-*a*

135 algorithms were implemented to the MODIS-Aqua and VIIRS-SNPP Level-2 data and then the
136 Level-2 data were remapped with Cylindrical projection at 2×2-km spatial resolution for the ES
137 and then used to generate monthly composite images.
138
139 **3. RESULTS**
140 ***3.1. Chl-a algorithms for Satellite Ocean Color Data***
141 The model-derived Chl-*a* data using the OC algorithms are generally well correlated to the in
142 situ Chl-*a* measurements but systematically overestimated in the lower Chl-*a* concentrations (<
143 ~1.0 mg/m^3) in all satellite ocean color sensors in the ES (Fig. 2). Mean (median & standard
144 deviation) ratio values of the model-derived Chl-*a* to the in situ Chl-*a* for OC3M, OC3V, OC4Me,
145 OC3G, and OC4G (Fig. 2(a)-(e)) are 1.45 (1.50 & 0.75), 1.41 (1.44 & 0.72), 1.59 (1.44 & 1.21),
146 1.44 (1.49 & 0.76), 1.42 (1.41 & 0.85), respectively. These results show the model-derived Chl-*a*
147 data are about 40% overestimated compared with the in situ Chl-*a* data. For more accurate
148 assessments in phytoplankton production in the ES, it is required to improve Chl-*a* algorithms in
149 the ES for the ocean color satellite data**.**
150 The SeaBASS Chl-*a* measurements are compared with the $R_{rs}(\lambda)$ ratios of blue to green bands
151 to derive an improved Chl-*a* algorithm for the ES. Figure 3 provides scatter plots of Chl-*a* with
152 MBR with 3 bands (OC3) for MODIS-Aqua (Fig. 3(a)), VIIRS-SNPP (Fig. 3(b)), and GOCI (Fig.
153 3(d)), and 4 bands (OC4) for OLCI (Fig. 3(c)) and GOCI (Fig. 3(e)). The 4th polynomial regression
154 lines between Chl-*a* and MBR from the OC3 and OC4 Chl-*a* algorithms are shown as blue dashed
155 lines. The MBR of OC3 and OC4 are noticeably not well correlated (higher) to Chl-*a* data in the
156 lower Chl-*a* range of about 0.1 - 1.0 mg/m^3.
157 After intensive analysis, we derived the best regression fits between Chl-*a* and MBR using
158 three band ratios (OC3x) for the five ocean color sensors (Table 2). Red lines in Fig. 3 indicate
159 the best 3rd polynomial regression fits. The Chl-*a* data are well correlated with MBR of 3 band

ratios for OC3M (r^2=0.73), OC3V (r^2=0.72), OC4Me (r^2=0.69), OC3G (r^2=0.72), and OC4G (r^2=0.72) in the ES. New-derived regression fits are well correlated to the Chl-*a* data, particularly in the low Chl-*a* range from 0.1 to 1.0 mg/m^3 while both the present and new-derived regression lines are quite similar in Chl-*a* higher than 1.0 mg/m^3 (except OC4Me). The revised ocean color Chl-*a* algorithms for the satellite ocean color sensors in the ES are shown in Table 2.

The model-derived Chl-*a* data using the new-derived algorithms are compared with the in situ Chl-*a* in figure 4. The results show that Chl-*a* data using the new algorithms are clearly improved in the ES compared with those using the OC algorithms, particularly in the low Chl-*a* values (0.1 to 1.0 mg/m^3). Mean (median & standard deviation) ratio values of the model-derived Chl-*a* to the in situ Chl-a for OC3M, OC3V, OC4Me, OC3G, and OC4G are 1.14 (1.07 & 0.66), 1.15 (1.05 & 0.69), 1.16 (1.09 & 0.76), 1.15 (1.04 & 0.70), 1.14 (1.06 & 0.69), respectively, inferring that the revised algorithms reduce uncertainties of the model-derived Chl-*a* for the satellite ocean color data from about 40% to 15% in the ES.

3.2. Comparison of Satellite-derived Chl-a Images

To compare the performance of the new-derived Chl-*a* algorithms in the ES, MODIS-Aqua and VIIRS-SNPP ocean color data were used. The present OC3 (OC3M and OC3V) and the revised algorithms were implemented to the MODIS-Aqua and the VIIRS-SNPP daily ocean color data in June 2016 as examples. Then, monthly composite images of the MODIS and VIIRS Chl-*a* were generated. Figure 5 shows the VIIRS-derived Chl-*a* images using the OC3V and the revised OC3V Chl-*a* algorithm in June 1st, 2016 covering a large area (~two thirds) of the ES. General

spatial distributions of the VIIRS-derived Chl-*a* using both OC3V and the new algorithm are very similar. However, compared with the VIIRS-derived Chl-*a* concentrations from the OC3V (Fig. 5(a)), those from the new algorithm are prominently lower in the middle and eastern area of the south ES, and eddies and patches (blue colors in Chl-*a* less than ~1.0 mg/m^3) are clearly shown (Fig. 5(b)). The monthly composite images of the VIIRS-derived Chl-*a* using the OC3V and the revised OC3V Chl-a algorithm in June, 2016 are also compared (Fig. 6). Similar to the daily Chl-*a* images, the lower Chl-a concentrations using the new algorithm revealed in the middle and eastern area of the south ES. In both the daily and monthly composite images, Chl-*a* concentrations and its spatial distributions from both OC3V and the new algorithms are very similar in the higher values (over 1.0 mg/m^3). In addition, histogram plots are generated for the VIIRS-derived daily Chl-*a* images in June 1st 2016 (Fig. 7(a)) and the monthly composite Chl-*a* images in June 2016 (Fig. 7(b)) using OC3V (blue dashed lines) and new algorithm (red lines). The histogram results provide that Chl-*a* concentrations using the new algorithm (peak in ~0.16 mg/m^3) are lower than those using OC3V (peak in ~0.25 mg/m^3) in Chl-*a* below ~1.0 mg/m^3, while Chl-*a* from both algorithms are almost identical in higher Chl-*a* (> ~1.0 mg/m^3).

MODIS-derived Chl-*a* images are also investigated for the same day and month with the VIIRS-derived Chl-*a* images shown in figures 5–7. The MODIS-derived Chl-*a* image using the OC3V (Fig. 8(a)) in June 1st, 2016 is compared with that using the revised OC3V algorithm (Fig. 8(b)). Similar to the pattern in the VIIRS-derived Chl-*a* images, lower Chl-*a* concentrations using the new algorithm (Chl-*a* < ~1.0 mg/m^3) are apparent in the middle and eastern area of the south the ES showing clearer eddies and patches, and Chl-*a* concentrations over about 1.0 mg/m^3 are very similar in the Chl-*a* images from both algorithms. Less valid areas in the MODIS Chl-*a* image compared with the VIIRS-derived Chl-*a* image are because of the slightly different passing times and coverages over the study area. The monthly composite images of the MODIS-derived Chl-*a* data in June, 2016 also show the very similar patterns (Fig. 9). Histogram results from the MODIS-

derived Chl-*a* images are almost consistent with those from the VIIRS-derived Chl-*a* images (Fig. 10). The MODIS-derived Chl-*a* concentrations using the new algorithm are lower with peak in ~0.16 mg/m^3 lower than those using OC3V with peak in ~0.25 mg/m^3, and the pattern of higher Chl-*a* (> ~1.0 mg/m^3) are very almost identical, but histogram shapes from the VIIRS- and MODIS-derived Chl-*a* data are slightly different. The difference could be because the passing times and coverages are slightly different in the study area as well as number of VIIRS and MODIS Level-2 data passing over the study area are different (total numbers of MODIS-Aqua and VIIRS-SNPP Level-2 files covering the ES in June 2016 are 122 and 131, respectively).

4. DISCUSSION and CONCLUSION

The present Chl-*a* OCx algorithms for the satellite ocean color data such as MODIS-Aqua, VIIRS-SNPP, OLCI, GOCI-1 and GOCI-2 in the global ocean have been assessed using the in situ radiometric and Chl-*a* measurements in the ES. The model-derived Chl-*a* data using the OCx algorithms are systematically overestimated in the lower Chl-*a* concentrations (< ~1.0 mg/m^3) in the ES with about 40% overestimation. The ES can be classified as Case I waters whose optical properties are mainly determined by phytoplankton concentration because the ES is a relatively deep ocean with mean depth of ~1,650 m and there is no major freshwater input from the rivers (Hong et al. 2008; Kim et al. 2016). The Chl-*a* OCx algorithms generally work well in the open ocean waters. However, it has been shown that there are optical differences in the oceans and these optical differences in the different regional oceans can be related to variations in phytoplankton community structures (sizes, species, accessory pigments) and the abundance in colored dissolved

organic matter (CDOM) (Szeto et al. 2011). Therefore, improved OCx-based Chl-*a* algorithms have been derived from the best 3rd polynomial regression fits between the in situ Chl-*a* and MBR data using the in situ measurements for the ES to provide more accurate estimation of phytoplankton biomass. Comparison results show that, indeed, the new Chl-*a* algorithms for the ES are improved for low Chl-*a* concentrations (between ~0.1 and 1.0 mg/m^3) with about 30% reduced uncertainties, while those are very similar to the original OCx algorithms in the higher Chl-*a* concentrations over ~1.0 mg/m^3. However, it should be noted that the in situ Chl-*a* measurements used in the revised Chl-*a* algorithms for the ES are all higher than 0.1 mg/m^3. Thus, the new Chl-*a* algorithms may not accurately represent Chl-*a* concentrations lower than 0.1 mg/m^3 although lower Chl-*a* concentrations are rarely reported in the ES.

This study has demonstrated that the revised regional Chl-a OCx algorithms can estimate more accurate Chl-a data using the satellite ocean color data (e.g., MODIS-Aqua, VIIRS-SNPP, OLCI, GOCI-1, and GOCI-2) and provide more reliable assessments in phytoplankton production and biogeochemical cycles in the ES.

Acknowledgments

The authors would like to acknowledge the US NASA Ocean Biology Processing Group for MODIS-Aqua and VIIRS-SNPP data and SeaBASS data (particularly, A. Mannino and M. Novak for HPLC data during the KORUS cruise). The research was supported by “ (KIMST-20140257 to JR) , “Development of Advanced Science and Technology for Marine Environmental Impact Assessment (KIMST-20210427 to JR)”, “ (KIMST-20220526 to JR) and “Development of technology using analysis of Ocean Satellite Images (KIMST-20210046 to SHL)” of Korea Institute of Marine Science & Technology Promotion (KIMST) funded by the

Ministry of Oceans and Fisheries (MOF), South Korea, the National Institute of Fisheries Science (R2023013) to HJ, and "Development of merging technology of geostationary ocean satellite data (P#2021-9)" by US NOAA-Korea MOF Joint Project Agreement Project.

This scientific results and conclusions, as well as any views or opinions expressed herein, are those of the author(s) and do not necessarily reflect those of NOAA or the US Department of Commerce.

REFERENCES

Ardyna, M., Arrigo, K. R., 2020. Phytoplankton Dynamics in a Changing Arctic Ocean. Nature Clim. Change 10: 892–903. doi:10.1038/s41558-020-0905-y.

Ashjian, C., Arone, R., Davis, C., Jones, B., Kahru, M., Lee, C., Mitchell, B. G., 2006. Biological Structure and Seasonality in the Japan/East Sea. Oceanography 19: 122–133. doi:10.5670/oceanog.2006.49.

Bailey, S., Franz, B., Werdell, P.J., 2010. Estimation of near-infrared waterleaving reflectance for satellite ocean color data processing. Optics Exp. 18: 7521-7527.

Chang, K.I., Ito, S., Mooers, C., Yoon, J. H., 2009. Observation and Modeling of the Ocean Circulation and Marine Ecosystem for CREAMS/PICES. J. Mar. Sys. 78: 195–199. doi:10.1016/j.jmarsys.2009.03.002.

Chen, C., Mao, Z., Han, G., Li, T., Wang, Z., Tao, B., 2017. Optimal PAR Intensity for Spring Bloom in the Northwest Pacific Marginal Seas. Ecol. Indicators 72: 428–435. doi:10.1016/j.ecolind.2016.08.044.

Han, I. S., Lee, J. S., 2020. Change the Annual Amplitude of Sea Surface Temperature due to Climate Change in a Recent Decade around the Korean Peninsula. J. Korean Soc. Mar. Env. Safety 26(3): 233–241. doi:10.7837/kosomes.2020.26.3.233.

Hong, G.H., Kim, Y.I., Baskaran, M., Kim, S.H., Chung, C.S., 2008. Distribution of ^{210}Po and export of organic carbon from the euphotic zone in the southwestern East Sea (Sea of Japan). J. Oceanogr. 64: 277-292.

Jo, C.O., Lee, J.Y., Park, K.A., Kim, Y.H., Kim, K.R., 2007. Asian Dust Initiated Early Spring Bloom in the Northern East/Japan Sea. Geophys. Res. Lett. 34: L05602. doi:10.1029/2006GL027395.

Jo, C.O., Park, S., Kim, Y.H., Park, K.A., Park, J.J., Park, M.K., Li, S., Kim, J.Y., Park, J.E., Kim, J.Y., Kim, K.R., 2014. Spatial Distribution of Seasonality of SeaWiFS Chlorophyll-a Concentrations in the East/Japan Sea. J. Mar. Sys. 139: 288–298. doi:10.1016/j.jmarsys.2014.07.004.

Jo, C.O., Ryu, J., Woo, S.Y., Lee, W.J., Kim, H.W., Choi, Y.S., 2021. Estimation of Ocean Export Production Ratios Based on Mixed Layer Depth and Satellite Chlorophyll Observations. Regional Studies Mar. Sci. 45: 101816. doi:10.1016/j.rsma.2021.101816.

Joo, H.T., Park, J.W., Son, S., Noh, J.H., Jeong, J.J., Kwak, J.H., Kang, C.K., Lee, S.H., 2014. Long-term annual primary production in the Ulleung Basin as a biological hot spot in the East/Japan Sea. J. Geophys. Res. 119, C10011. Doi:10.1002/2014JC009862.

Joo, H.T., Son, S., Park, J.W., Kang, J.J., Jeong, J.J., Kang, C.K., Lee, S.H., 2017. Small phytoplankton contribution to total primary production in the highly productive Ulleung Basin in the East/Japan Sea. Depp-Sea Res. II. 143: 54-61.

Joo, H.T., Son, S., Park, J.W., Kang, J.J., Jeong, J.J., Lee, C.I., Kang, C.K., Lee, S.H., 2016. Long-Term Pattern of Primary Productivity in the East/Japan Sea Based on Ocean Color Data Derived from MODIS-Aqua. Remote Sens. 8(1): 25. doi:10.3390/rs8010025.

Kim, K., Chang, K.I., Kang, D.J., Kim, Y.H., Lee, J. H., 2008. Review of Recent Findings on the Water Masses and Circulation in the East Sea (Sea of Japan). J. Oceanogr. 64:721–735. doi:10.1007/s10872-008-0061-x.

Kim, K., Kim, K.R., Min, D.H., Volkov, Y., Yoon, J.H., Takematsu, M., 2001. Warming and Structural Changes in the East(Japan) Sea: a Clue to Future Changes in Global Oceans? Geophys. Res. Lett. 28:3293–3296. doi:10.1029/2001GL013078.

Kim, K., Lee, S., Park, K., Park, J., Suh, Y., Lee, D., Kang, D., Chang, K., 2016. General Introduction. Oceanography of the East Sea (Japan Sea). Edited by Chang et al., Springer. doi:10.1007/978-3-319-22720-7.

Kim, S.W., Saitoh, S.I., Ishizaka, J., Isoda, Y., Kishino, M., 2000. Temporal and Spatial Variability of Phytoplankton Pigment Concentrations in the Japan Sea derived from CZCS Images. J. Oceanogr. 56: 527–538. doi:10.1023/A:1011148910779.

KIOST, 2021. Chlorophyll concentration algorithm for GOCI-II data. Korea Ocean Satellite Center (KOSC) of Korea Institute of Ocean Science and Technology (KIOST).

Lee, D., An, Y., Park, K.J., Kim, H.W., Lee, D., Joo, H., Oh, Y.G., Kim, S.M., Kang, C., Lee, S.H., 2017. Spatial distribution of common Mink whale (*Balaenoptera acutorostrata*) as an indication of a biological hotspot in the East Sea. Deep-Sea Res. II. 143: 91-99.

Lee, D., Kang, J., Jo, N., Kim, K., Jang, H., Kim, M., Kim, Y., Park, S., Son, S., Kwon, J., Yun, M., Kang, C., Lee, S.H., 2022. Variations in phytoplankton primary production driven by the Pacific Decadal Oscillation based on ocean color data in the East/Japan Sea, South Korea. J. Geophys. Res.: Biogeosciences. 127, e2022JG007094. https://doi.org/10.1029/2022JG007094.

Lee, D., Son, S., Kim, W., Lee, S.H., 2018. Spatio-temporal variability of the habitat suitability index for Chub Mackerel (*Scomber japonicas*) in the East/Japan Sea and the South Sea of South Korea. Remote Sensing. 10(6), 938, doi:10.3390/rs10060938.

Lee, D., Son, S., Lee, C, Kang, C., Lee, S.H., 2019. Spatio-temporal variability of the habitat suitability index for the Todarodes pacificus (Japanese Common Squid) around South Korea. Remote Sensing. 11(23), 2720, doi:10.3390/rs11232720.

Lee, J.Y., Kang, D.J., Kim, I.N., Rho, T., Lee, T., 2009. Spatial and Temporal Variability in the Pelagic Ecosystem of the East Sea (Sea of Japan): A review. J. Mar. Sys. 78: 288–300. doi:10.1016/j.jmarsys.2009.02.013.

Lee, S.H., Son, S., Dahms, H., Park, J., Lim, J., Noh, J., Kwon, J., Kang, C., 2014. Decadal changes of phytoplankton chlorophyll-a in the East Sea/Sea of Japan. Oceanology 54(6): 771–779.

330 Maúre, E. R., Ishizaka, J., Sukigara, C., Mino, Y., Aiki, H., Matsuno, T., Tomita, H., Goes, J.,
331 Gomes, H., 2017. Mesoscale Eddies Control the Timing of Spring Phytoplankton Blooms: A Case
332 Study in the Japan Sea. Geophys. Res. Lett. 44: 11115–11124. doi:10.1002/2017GL074359.

333 Morel, A., Antoine, D., 2011. Pigment index retrieval in Case 1 waters Algorithm Technical
334 Baseline Document 2.9. European Space Agency (PO-TN-MEL-GS-0005).

335 Morel, A., Gentili, B., Claustre, H., Babin, M., Bricaud, A., Ras, J., Tieche, F., 2007a. Optical
336 properties of the "clearest" natural waters. Limnol. Oceanogr. 52: 217–229.

337 Morel, A., Huot, Y., Gentili, B., Werdell, P.J., Hooker, S.B., Franz, B.A., 2007b. Examining the
338 consistency of products derived from various ocean color sensors in open ocean (Case 1) waters
339 in the perspective of a multi-sensor approach. Remote Sens. Env. 111: 69–88.
340 doi:10.1016/j.rse.2007.03.012.

341 O'Reilly, J.E., Maritorena, S., Mitchell, G., Siegel, D., Carder, K., Garver, S., Kahru, M., McClain,
342 C., 1998. Ocean color chlorophyll algorithms for SeaWiFS. J. Geophys. Res. 103: 24937-24953.

343 O'Reilly, J.E., Maritorena, S., Sigel, D., O'Brien, M., Toole, D., Mitchell, G., Kahru, M., et al.,
344 2000. Ocean color chlorophyll a algorithms for SeaWiFS, OC2 and OC4: version 4. SeaWiFS
345 Postlaunch Technical Report Series, NASA Tech. Memo. 2000-206892, p8-22, S. Hooker and E.
346 Firestone, Eds., NASA Goddard Space Flight Center, Greenbelt, MD, USA.

347 Sapiano, M.R.P., Brown, C.W., Schollaert, S., Vargas, M., 2012. Establishing a Global
348 Climatology of Marine Phytoplankton Phenological Characteristics. J. Geophys. Res.
349 117:C08026. doi:10.1209/2012JC007958.

Son, S., Campbell, J., Dowell, M., Yoo, S., Noh, J., 2005. Primary production model using ocean color remote sensing in the Yellow Sea. Mar. Ecol. Prog. Ser. 303: 91–103.

Stumpf, R., Arnone, R., Gould, R., Martinolich, P., Ransibrahmanakul, V., 2003. A partially coupled ocean-atmosphere model for retrieval of water leaving radiance from SeaWiFS in coastal waters. Chapter 9 in: Patt, F.S., et al.: Algorithm updates for the fourth SeaWiFS data processing. NASA Tech. Memo. 2003-206892, S.B. Hooker, E.R. Firestone, Eds., NASA Goddard Space Flight Center, Greenbelt, Maryland, pp51-59.

Szeto, M., Werdell, P.J., Moore, T.S., Campbell, J.W., 2011. Are the world's oceans optically different. J. Geophys. Res. 116: C00H04. doi:10.1209/2011JC007230.

Werdell, P.J., Bailey 2002, S.W., The SeaWiFS Bio-optical Archive and Storage System (SeaBASS): Current architecture and implementation. NASA Tech. Memo. 2002-211617, G.S. Fargion and C.R. McClain, Eds., NASA Goddard Space Flight Center, Greenbelt, Maryland, 45pp.

Werdell, P.J., Bailey, S.W., Fargion, G.S., Pietras, C., Knobelspiesse, K.D., Feldman, G.C., McClain, C.R., 2003. Unique data repository facilitates ocean color satellite validation. EOS Trans. AGU, 84, 377.

Yamada, K., Ishizaka, J., Yoo, S., Kim, H.C., Chiba, S., 2004. Seasonal and Interannual Variability of Sea Surface Chlorophyll a Concentration in the Japan/East (JES). Prog. Oceanogr. 61: 193–211. doi:10.1016/j.pocean.2004.06.001.

Yamada, K., Ishizaka, I., Nagata, H., 2005. Spatial and Temporal Variability of Satellite Primary Production in the Japan Sea from 1998 to 2002. J. Oceanogr. 61: 857–869. doi:10.1007/s10872-006-0005-2.

Table 1. The Chl-a OCx algorithms for MODIS-Aqua and VIIRS-SNPP (O'Reilly et al. 1998, 2000; https://oceancolor.gsfc.nasa.gov/atbd/chlor_a/), OLCI (Morel and Antoine 2011; Morel et al. 2007a, 2007b), and GOCI-1 and GOCI-2 (KIOST 2021).

Algorithm	Sensor	X	Chl-*a*
OC3M	MODIS-Aqua	$log\left[\frac{Max\left(R_{rs}(443),\ R_{rs}(488)\right)}{R_{rs}(547)}\right]$	$10^{(0.2424-2.7425X+1.8017X^2+0.0015-1.2280)}$
OC3V	VIIRS-SNPP	$log\left[\frac{Max\left(R_{rs}(443),\ R_{rs}(486)\right)}{R_{rs}(551)}\right]$	$10^{(0.4503-3.2595X+3.5227X^2-3.3594+0.9496)}$
OC4Me	OLCI	$log\left[\frac{Max\left(R_{rs}(443),\ R_{rs}(490),\ R_{rs}(510)\right)}{R_{rs}(560)}\right]$	$10^{(0.2228-2.4683X+1.5867X^2-0.4275-0.7768)}$
OC3G	GOCI-1, GOCI-2	$log\left[\frac{Max\left(R_{rs}(443),\ R_{rs}(490)\right)}{R_{rs}(555)}\right]$	$10^{(0.2515-2.3798X+1.5823X^2-0.6372-0.5692)}$
OC4G	GOCI-1, GOCI-2	$log\left[\frac{Max\left(R_{rs}(443),\ R_{rs}(490),\ R_{rs}(510)\right)}{R_{rs}(555)}\right]$	$10^{(0.3272-2.9940X+2.7218X^2-1.2259-0.5683)}$

Table 2. The revised Chl-*a* algorithms for the ES.

Algorithm	Sensor	X	Chl-*a*
OC3M	MODIS-Aqua	$log\left[\frac{Max\left(R_{rs}(443),\ R_{rs}(488)\right)}{R_{rs}(547)}\right]$	$10^{(0.2054-2.7557X+1.0013X^2-0.5140)}$
OC3V	VIIRS-SNPP	$log\left[\frac{Max\left(R_{rs}(443),\ R_{rs}(486)\right)}{R_{rs}(551)}\right]$	$10^{(0.2724-2.5283X+1.3375X^2-1.1431)}$
OC4Me	OLCI	$log\left[\frac{Max\left(R_{rs}(443),\ R_{rs}(490),\ R_{rs}(510)\right)}{R_{rs}(560)}\right]$	$10^{(0.2169-2.5984X+1.0546X^2-0.7604)}$
OC3G	GOCI-1, GOCI-2	$log\left[\frac{Max\left(R_{rs}(443),\ R_{rs}(488)\right)}{R_{rs}(555)}\right]$	$10^{(0.2289-2.4851X+1.1496X^2-0.8978)}$
OC4G	GOCI-1, GOCI-2	$log\left[\frac{Max\left(R_{rs}(443),\ R_{rs}(490),\ R_{rs}(510)\right)}{R_{rs}(555)}\right]$	$10^{(0.2438-2.7800X+2.1076X^2-1.6199)}$

385 **Figure Captions**

386 **Figure 1**. Map of the East/Japan Sea. Pink circles indicate the locations of the in situ
387 measurements.

388 **Figure 2**. Comparisons of the in situ Chl-*a* measurements in the ES with the model-derived Chl-*a*
389 using (a) OC3M, (b) OC3V, (c) OC4Me, (d) OC3G, and (e) OC4G algorithms.

390 **Figure 3**. Comparison results of the in situ Chl-*a* data with the maximum band ratio of (a) OC3M,
391 (b) OC3V, (c) OC4Me, (d) OC3G, and (e) OC4G. Red straight lines indicate the best 3rd
392 polynomial fits of Chl-*a* versus the maximum band ratio, while the blue dashed lines
393 indicate the original relationship of OC3M, OC3V, OC4Me, OC3G, and OC4G.

394 **Figure 4**. Comparisons of the in situ Chl-*a* measurements in the ES with the model-derived Chl-*a*
395 using the new revised Chl-*a* (a) OC3M, (b) OC3V, (c) OC4Me, (d) OC3G, and (e) OC4G
396 algorithms.

397 **Figure 5**. Daily images of VIIRS-SNPP Chl-a in June 1st, 2016 derived using (a) OC3V and (b)
398 the new Chl-*a* algorithm for VIIRS-SNPP.

399 **Figure 6**. Monthly composite images of the MODIS-SNPP Chl-a in June 2016 derived using (a)
400 OC3V and (b) the new Chl-*a* algorithm for VIIRS-SNPP.

401 **Figure 7**. Histogram results of VIIRS-SNPP (a) daily Chl-a data in June 1st, 2016 and (b) monthly
402 composite Chl-a data in June 2016 derived using OC3V (blue dashed lines) and the new
403 Chl-*a* algorithm for VIIRS-SNPP (red lines).

404 **Figure 8**. Daily images of MODIS-Aqua Chl-*a* in June 1st, 2016 derived using (a) OC3V and (b)
405 the new Chl-*a* algorithm for MODIS-Aqua.

406 **Figure 9**. Monthly composite images of the MODIS-Aqua Chl-*a* in June 2016 using (a) OC3V
407 and (b) the new Chl-*a* algorithm for MODIS-Aqua.

408 **Figure 10**. Histogram results of MODIS-Aqua (a) daily Chl-a data in June 1st, 2016 and (b)
409 monthly composite Chl-a data in June 2016 derived using OC3V (blue dashed lines) and
410 the new Chl-*a* algorithm for MODIS-Aqua (red lines).

411

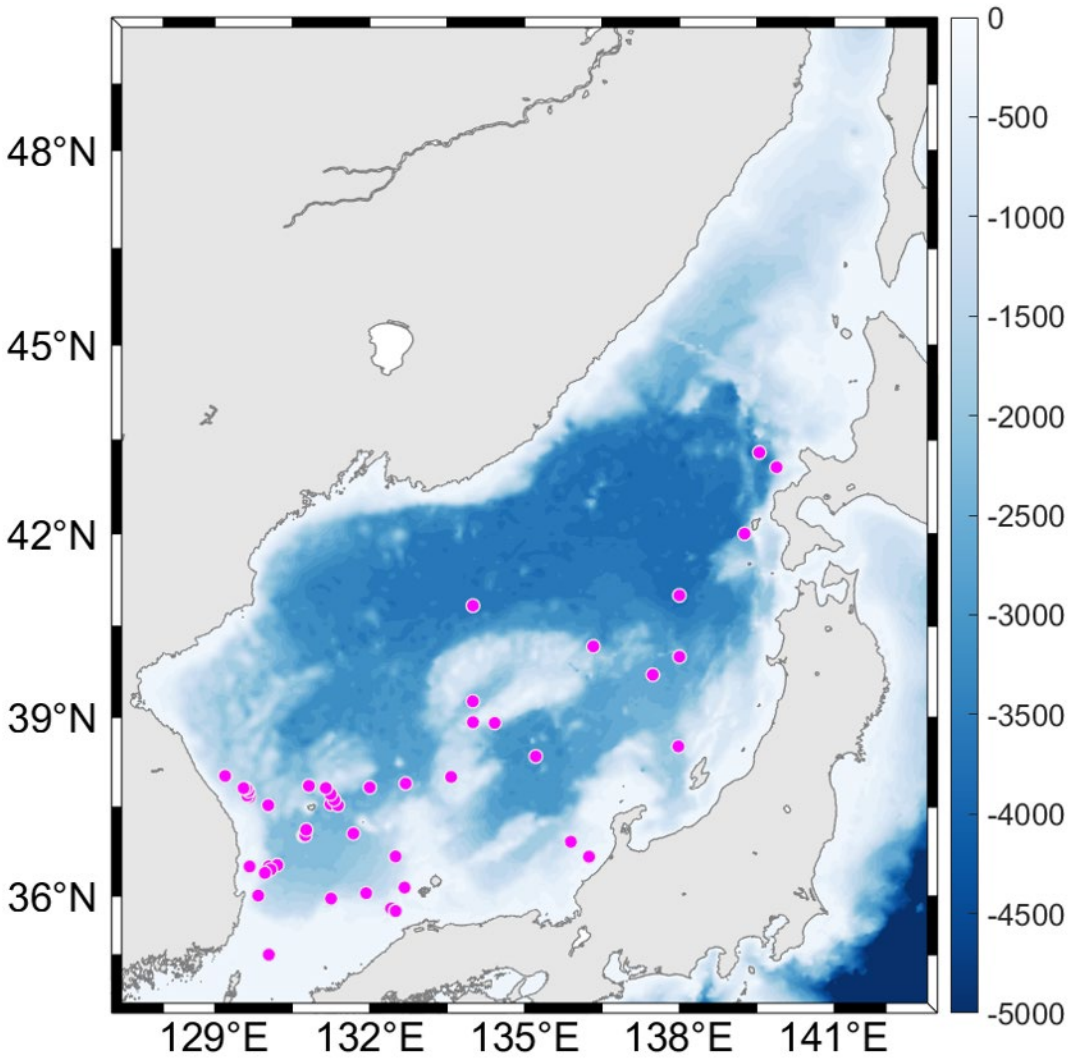
48°N
45°N
42°N
39°N
36°N
129°E
132°E
135°E
138°E
141°E
0
-500
-1000
-1500
-2000
-2500
-3000
-3500
-4000
-4500
-5000

412

413 **Fig. 1**

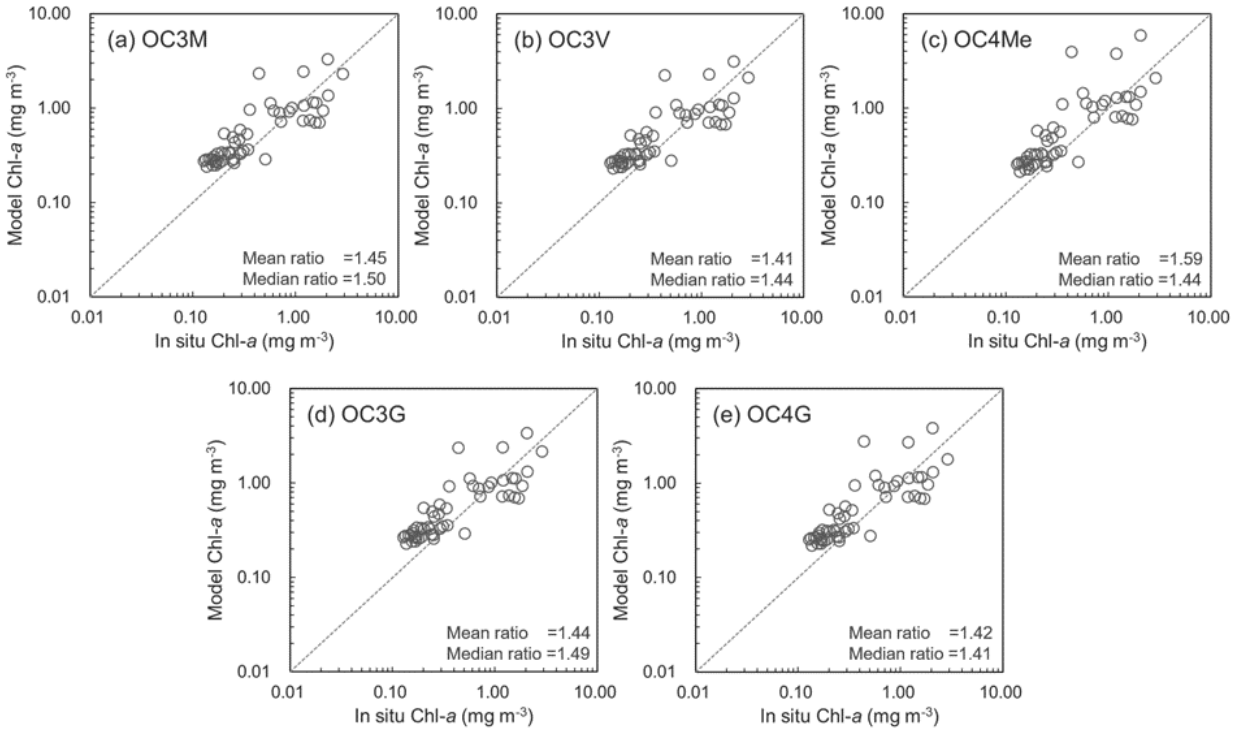
(a) OC3M
Mean ratio =1.45
Median ratio =1.50
(b) OC3V
Mean ratio =1.41
Median ratio =1.44
(c) OC4Me
Mean ratio =1.59
Median ratio =1.44
(d) OC3G
Mean ratio =1.44
Median ratio =1.49
(e) OC4G
Mean ratio =1.42
Median ratio =1.41
Model Chl-a (mg m-3)
In situ Chl-a (mg m-3)
0.01
0.10
1.00
10.00

414

415 **Fig. 2**

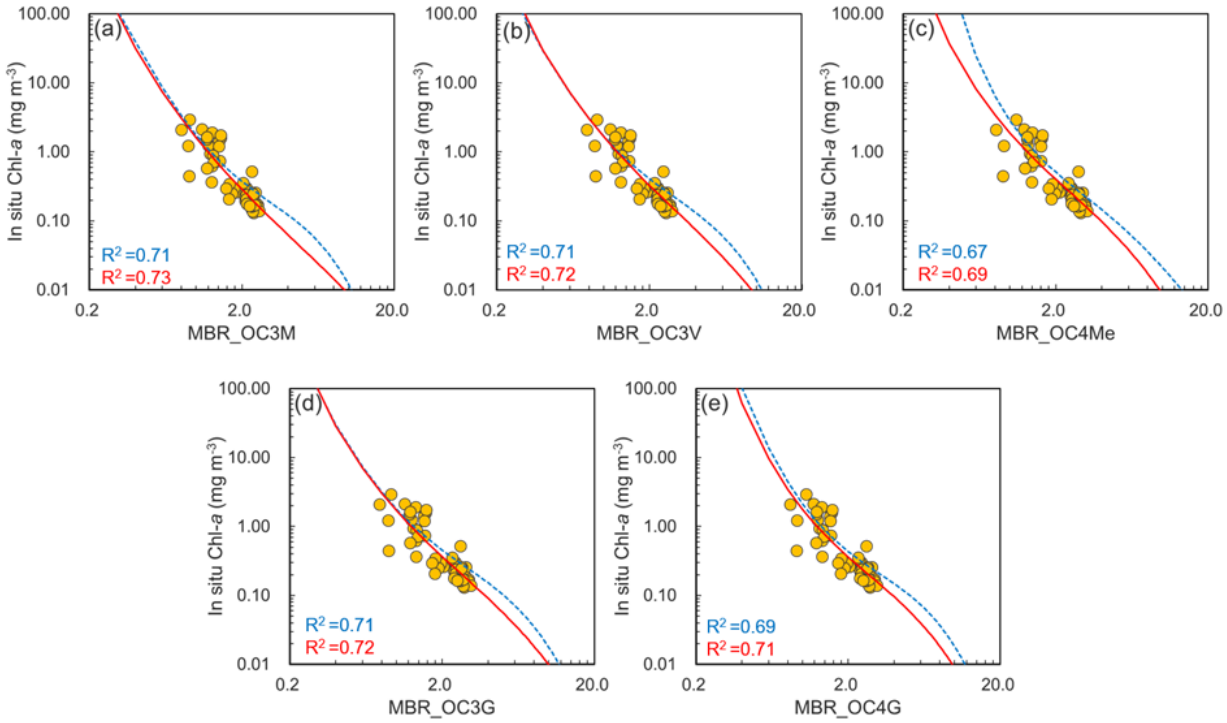
(a)
(b)
(c)
(d)
(e)
In situ Chl-a (mg m-3)
100.00
10.00
1.00
0.10
0.01
0.2
2.0
20.0
MBR_OC3M
MBR_OC3V
MBR_OC4Me
MBR_OC3G
MBR_OC4G
R2 =0.71
R2 =0.73
R2 =0.71
R2 =0.72
R2 =0.67
R2 =0.69
R2 =0.71
R2 =0.72
R2 =0.69
R2 =0.71

416

417 **Fig. 3**

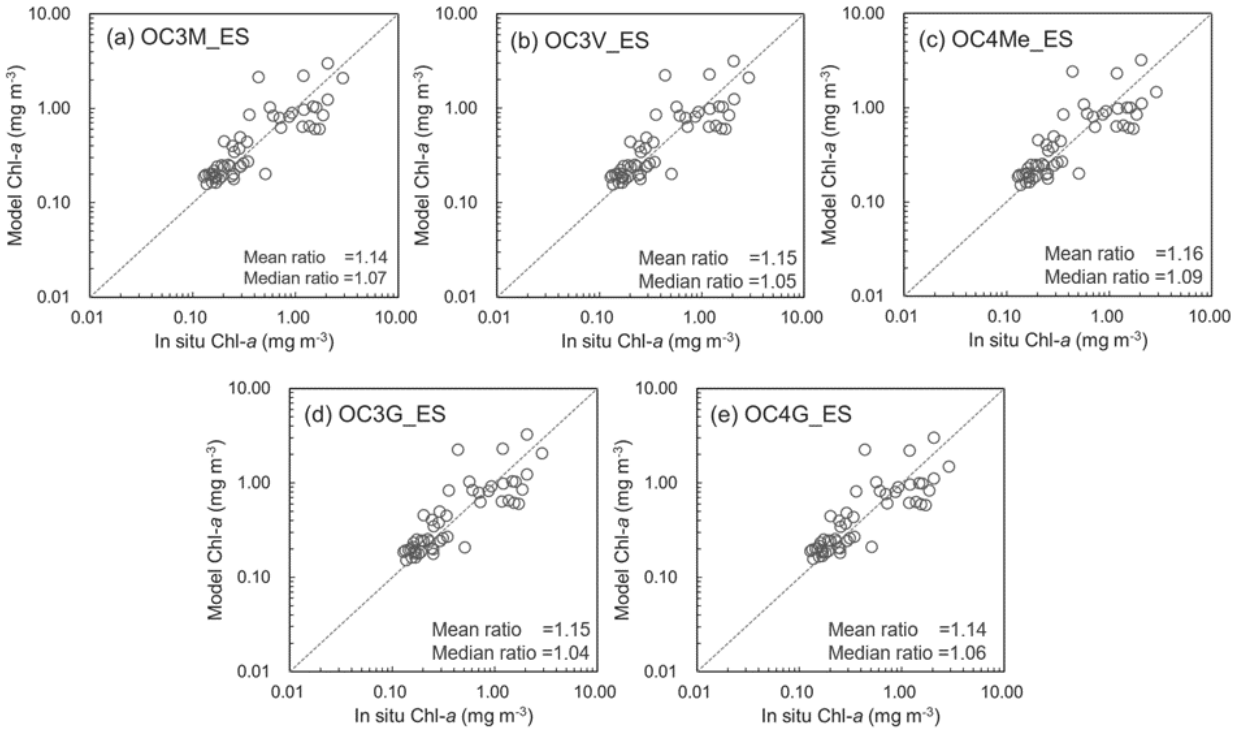
(a) OC3M_ES
Mean ratio =1.14
Median ratio =1.07
(b) OC3V_ES
Mean ratio =1.15
Median ratio =1.05
(c) OC4Me_ES
Mean ratio =1.16
Median ratio =1.09
(d) OC3G_ES
Mean ratio =1.15
Median ratio =1.04
(e) OC4G_ES
Mean ratio =1.14
Median ratio =1.06
Model Chl-a (mg m-3)
In situ Chl-a (mg m-3)
0.01
0.10
1.00
10.00

418

419 **Fig. 4**

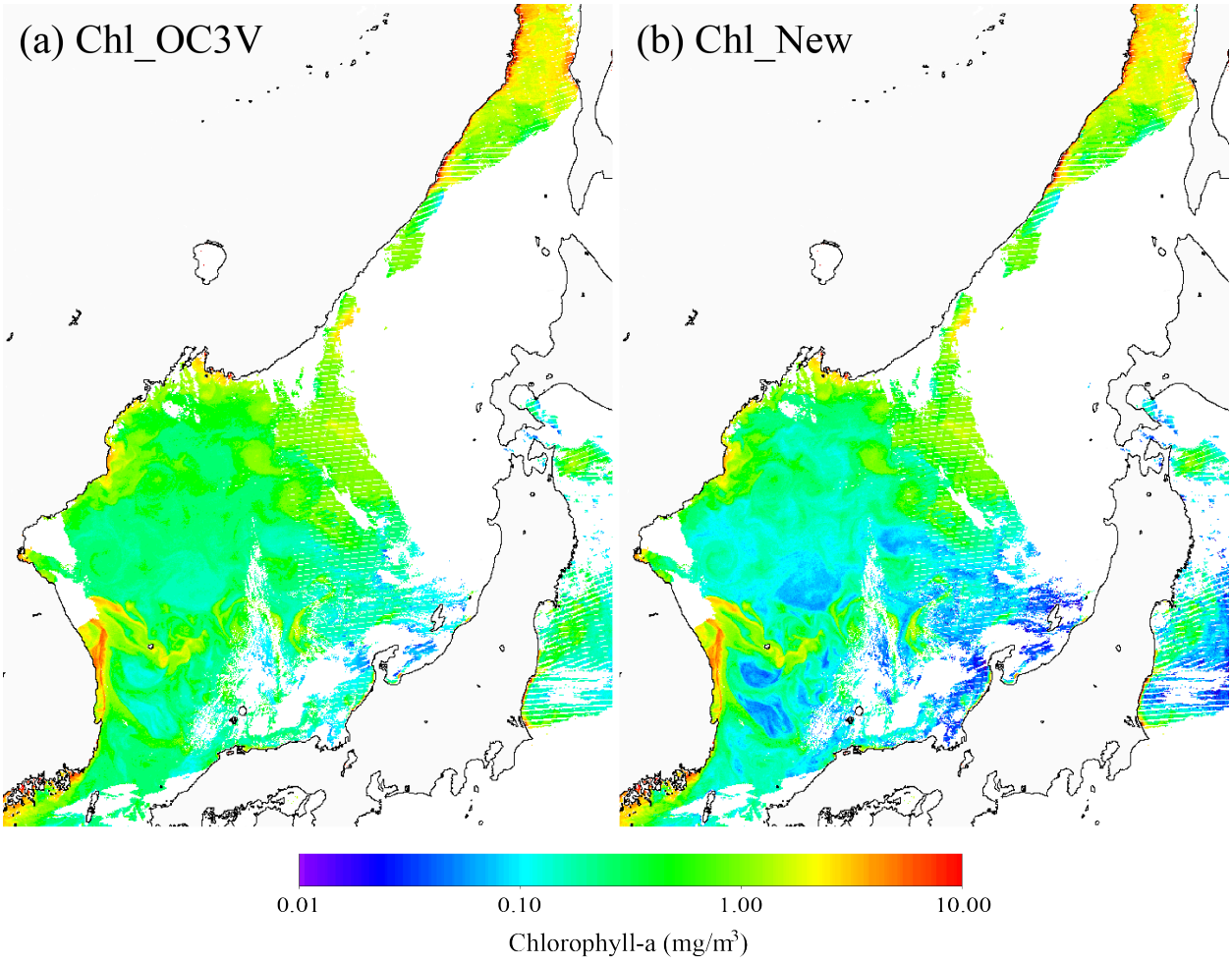

420

421 **Fig. 5**

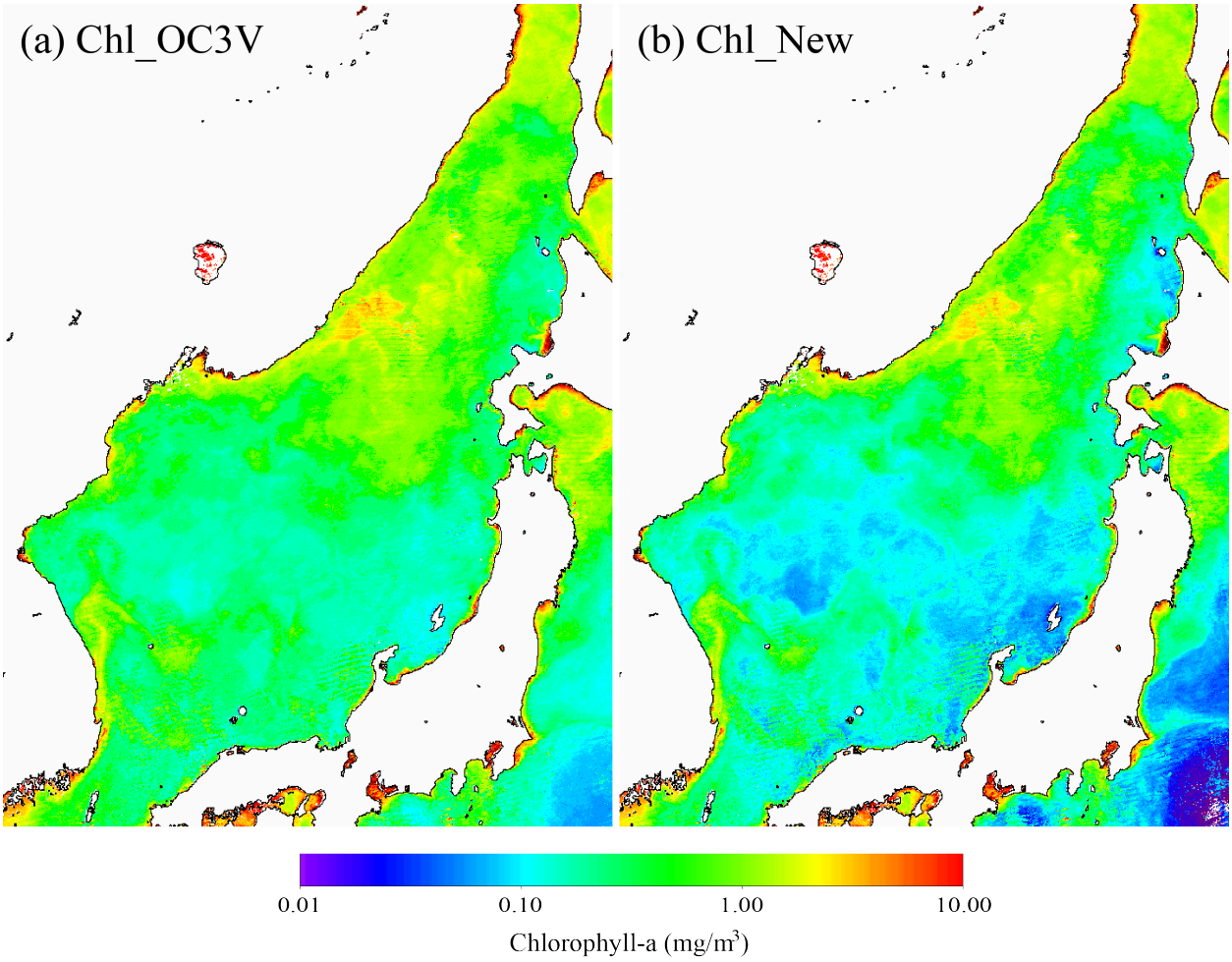

422

423 **Fig. 6**

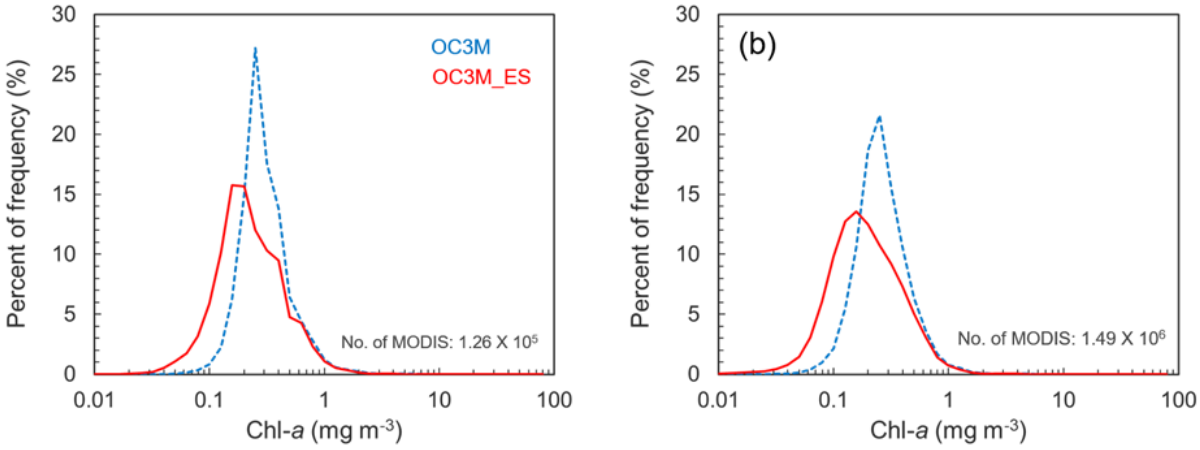
OC3M
OC3M_ES
No. of MODIS: 1.26 X 10⁵
Percent of frequency (%)
Chl-a (mg m⁻³)
(b)
No. of MODIS: 1.49 X 10⁶
Percent of frequency (%)
Chl-a (mg m⁻³)

424

425 **Fig. 7**

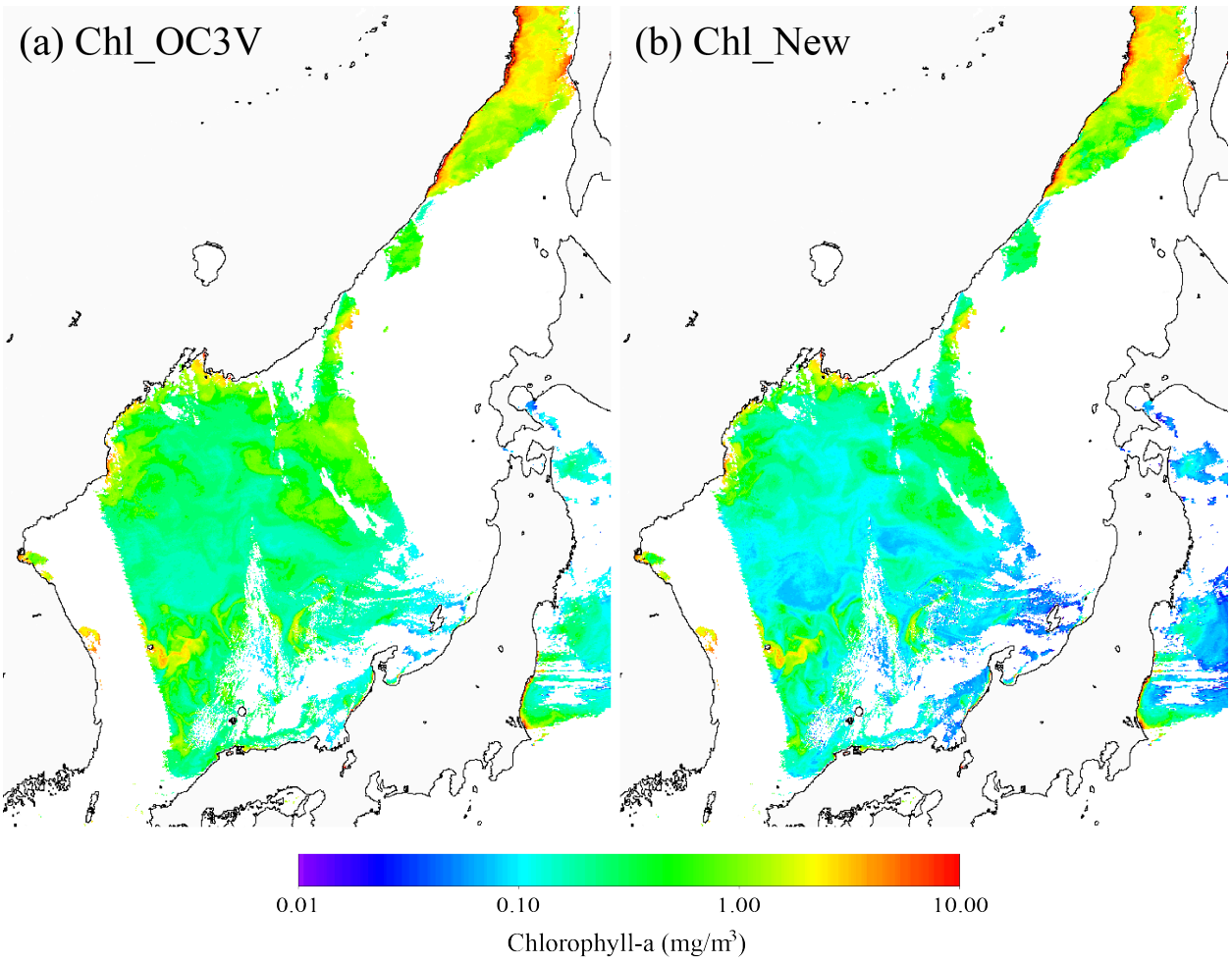

426

427

Fig. 8

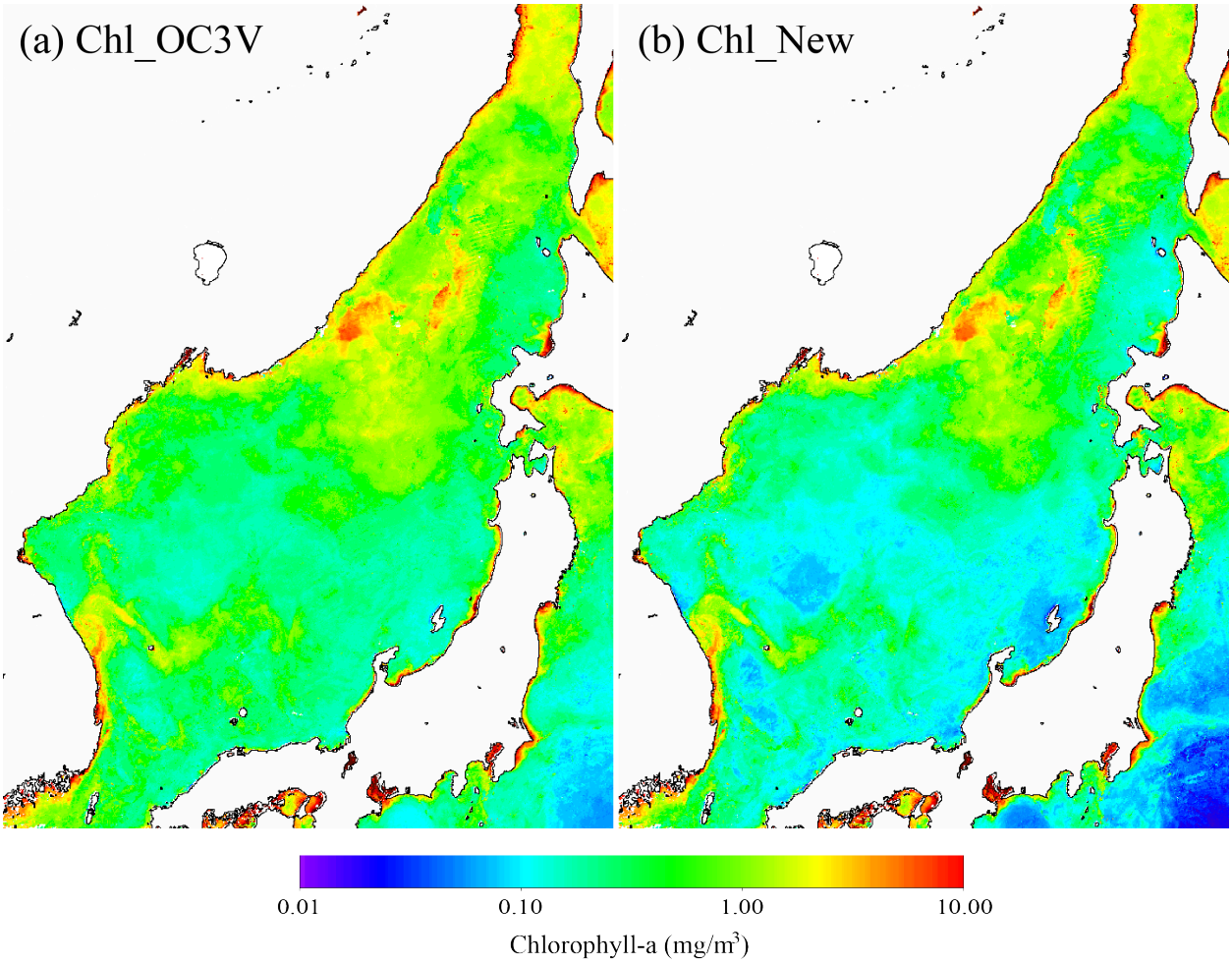

428

429 **Fig. 9**

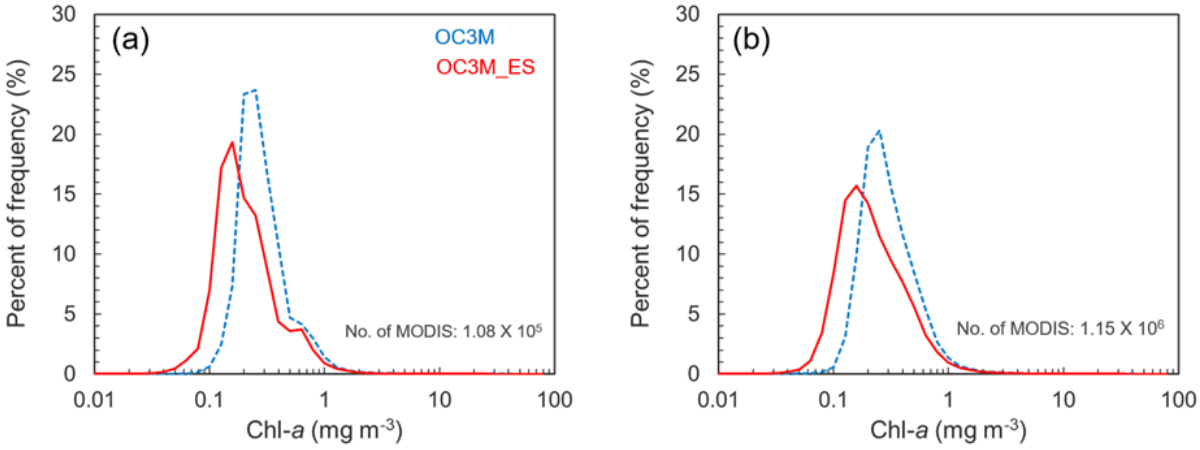

430

431 **Fig. 10**

432